Supporting Information

Determining Brown's characteristic curves using molecular simulation

*Maximilian Urschel, Simon Stephan**

Laboratory of Engineering Thermodynamics (LTD), TU Kaiserslautern, Kaiserslautern, 67663, Germany

Simon.Stephan@rptu.de

2023-02-04

The Supporting Information of the publication *Determining Brown's characteristic curves using molecular simulation* contains:

I. Detailed discussion of the results for the Lennard-Jones fluid

II. Simulation details and results for toluene, ethane, propane, and ethanol

III. Results for the Lennard-Jones truncated and shifted fluid

IV. Testing the linearity-law for the Zeno curve

V. Electronic Supporting Information containing implementation of the proposed computational procedure

VI. Electronic Supporting Information containing the primary data from the simulation results

Detailed discussion of results for the Lennard-Jones fluid

The results for the Lennard-Jones fluid are discussed in detail here regarding: (A) the fits of the polynomial curves, (B) comparison of approaches using data directly sampled in *ms*2, and (C) detailed comparison to literature data for the Charles curve.

Results of fitted curves for evaluation of characteristic curve state points

The results of the fitted second-order polynomial curves for the evaluation of the characteristic curve state points are shown in Figs. S1 - S4 for the four characteristic curves.

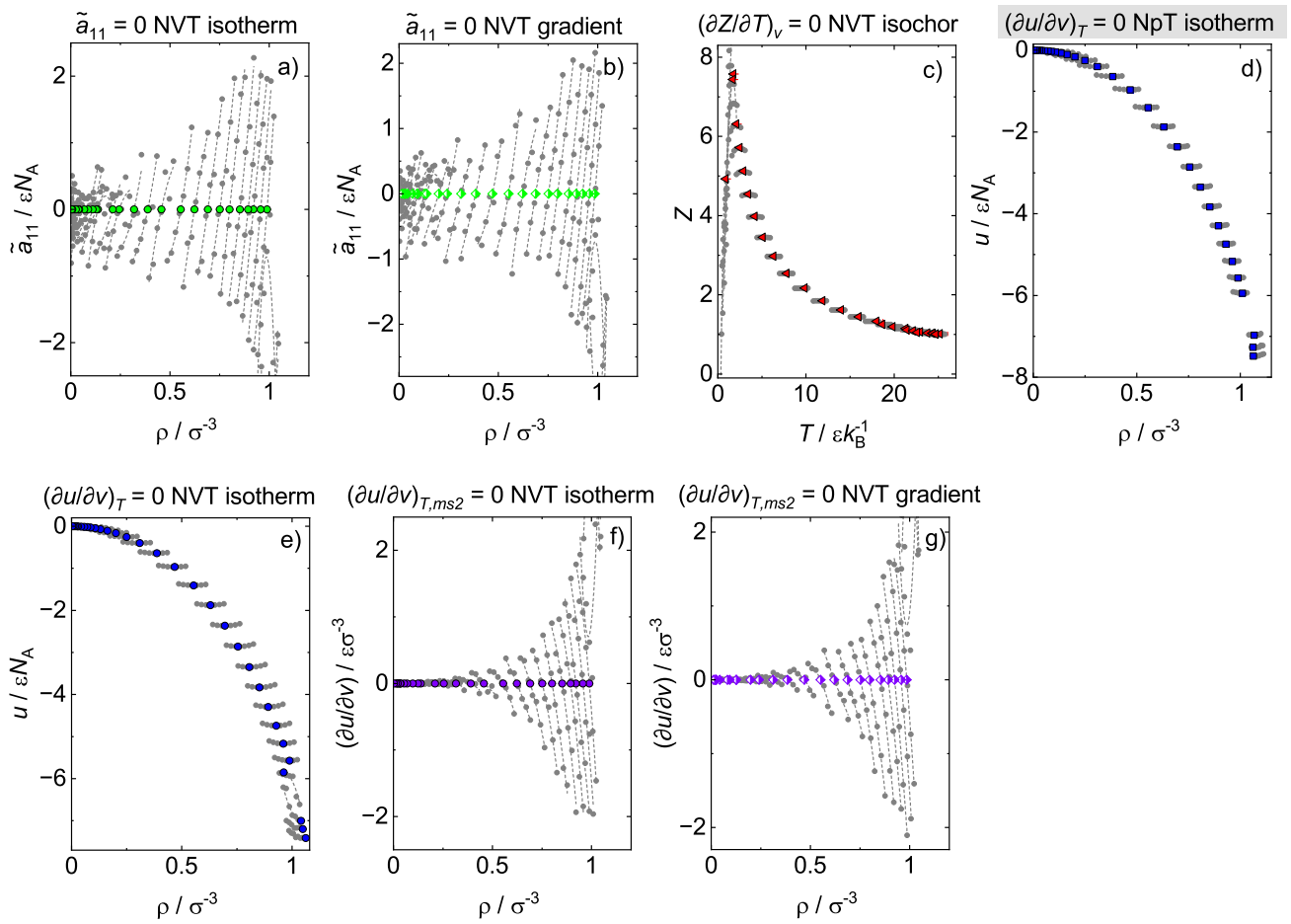

Figure S1: Results for the Zeno curve for the Lennard-Jones fluid. Fitted second-order polynomial curves and obtained state points. Grey dots indicate the simulation results, dotted lines indicate second-order polynomial fits, and colored symbols indicate the state points derived from the fitted curve. The overall most favorable approach is highlighted by the gray frame.

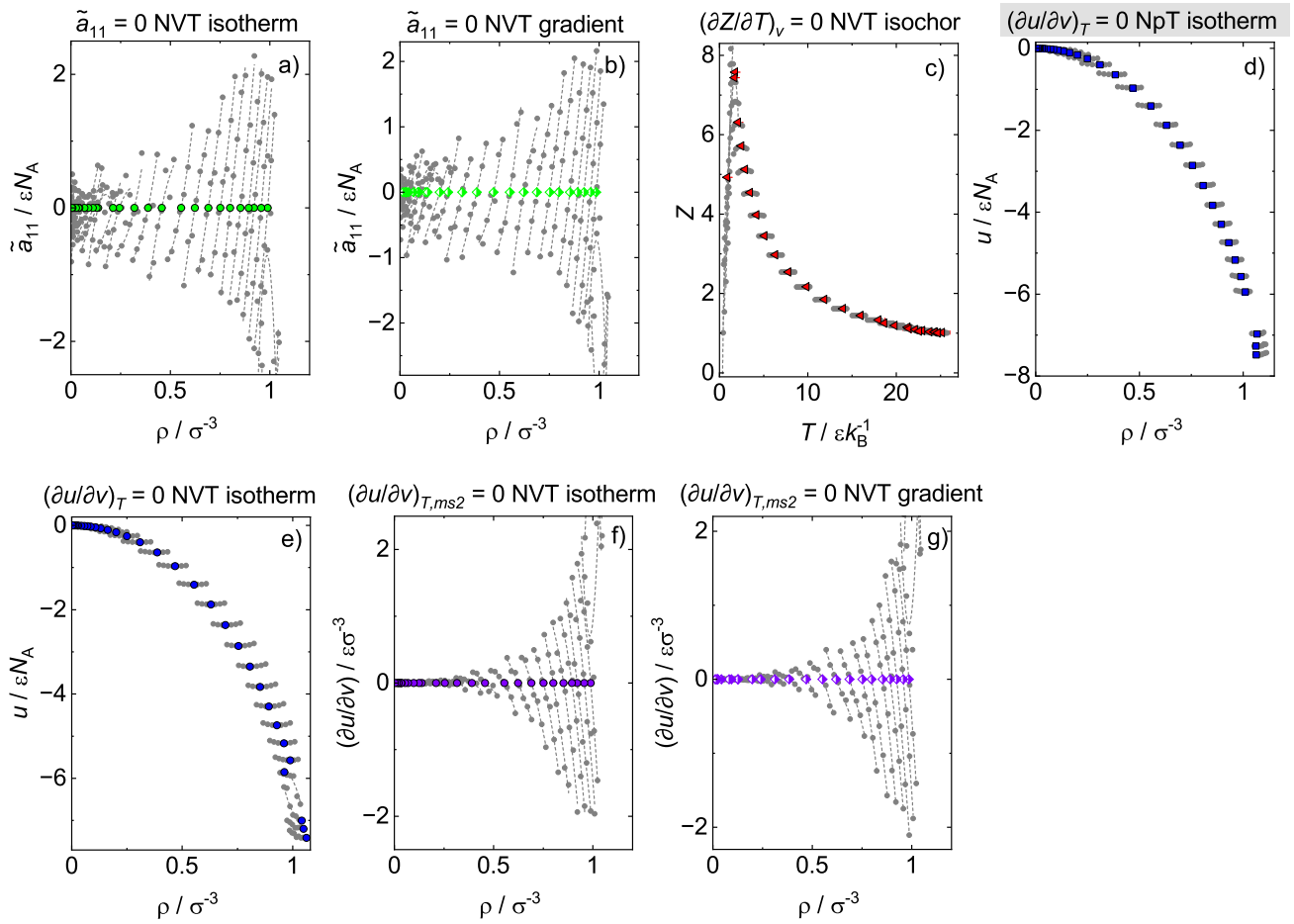

Figure S2: Results for the Amagat curve for the Lennard-Jones fluid. Fitted second-order polynomial curves and obtained state points. Grey dots indicate the simulation results, dotted lines indicate second-order polynomial fits, and colored symbols indicate the state points derived from the fitted curve. The overall most favorable approach is highlighted by the gray frame.

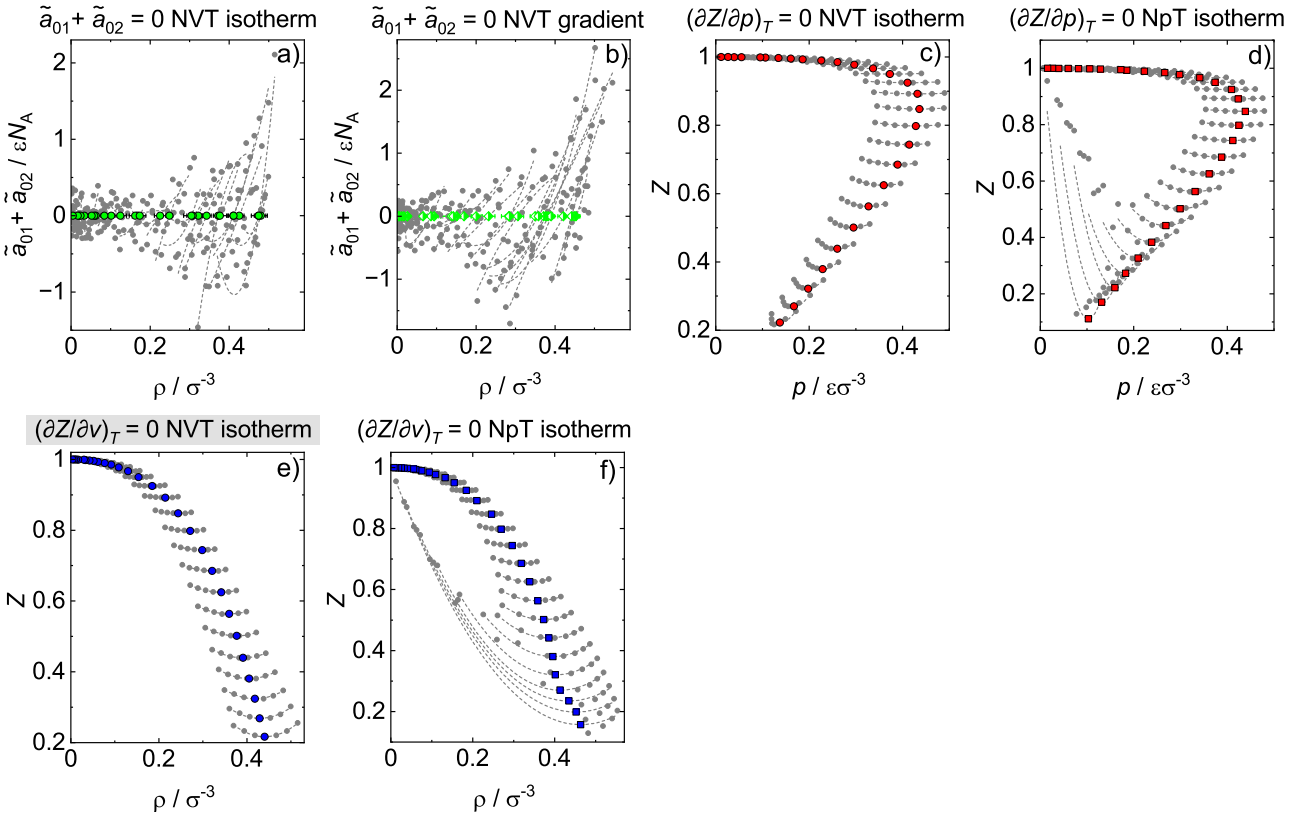

Figure S3: Results for the Boyle curve for the Lennard-Jones fluid. Fitted second-order polynomial curves and obtained state points. Grey dots indicate the simulation results, dotted lines indicate second-order polynomial fits, and colored symbols indicate the state points derived from the fitted curve. The overall most favorable approach is highlighted by the gray frame.

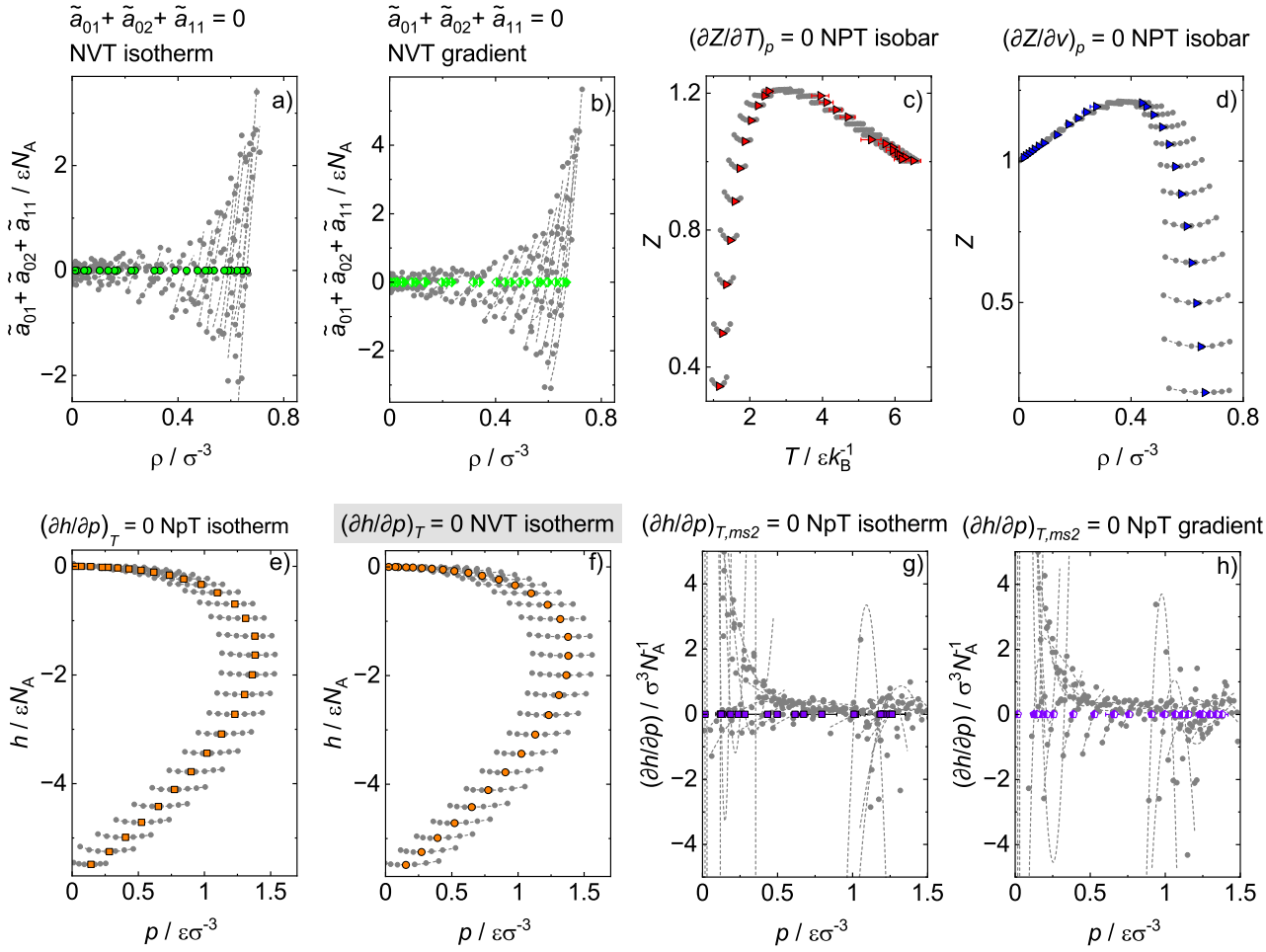

Figure S4: Results for the Charles curve for the Lennard-Jones fluid. Fitted second-order polynomial curves and obtained state points. Grey dots indicate the simulation results, dotted lines indicate second-order polynomial fits, and colored symbols indicate the state points derived from the fitted curve. The overall most favorable approach is highlighted by the gray frame.

Comparison of approaches using data directly sampled in *ms*2

Fig. S5 shows the comparison of the results using the condition $(\partial u/\partial v)_T = 0$ for the direct output of $(\partial u/\partial v)$ for NVT simulations provided by *ms*2 and the approach based on the evaluation of the data of u over v. The results determined by the direct sampling approaches exhibit significantly larger scattering and statistical uncertainties compared to the indirect approaches. Hence, the indirect approach is favored.

Fig. S6 shows the equivalent results for the Charles curve, i.e. the comparison of the results using the direct output of $(\partial h/\partial p)$ provided by *ms*2 and the approach based on the evaluation of the data of h over p. Again, the results obtained from the direct approaches exhibit significantly larger scattering and statistical uncertainties compared to the indirect approaches. Therefore, the indirect approach is favored.

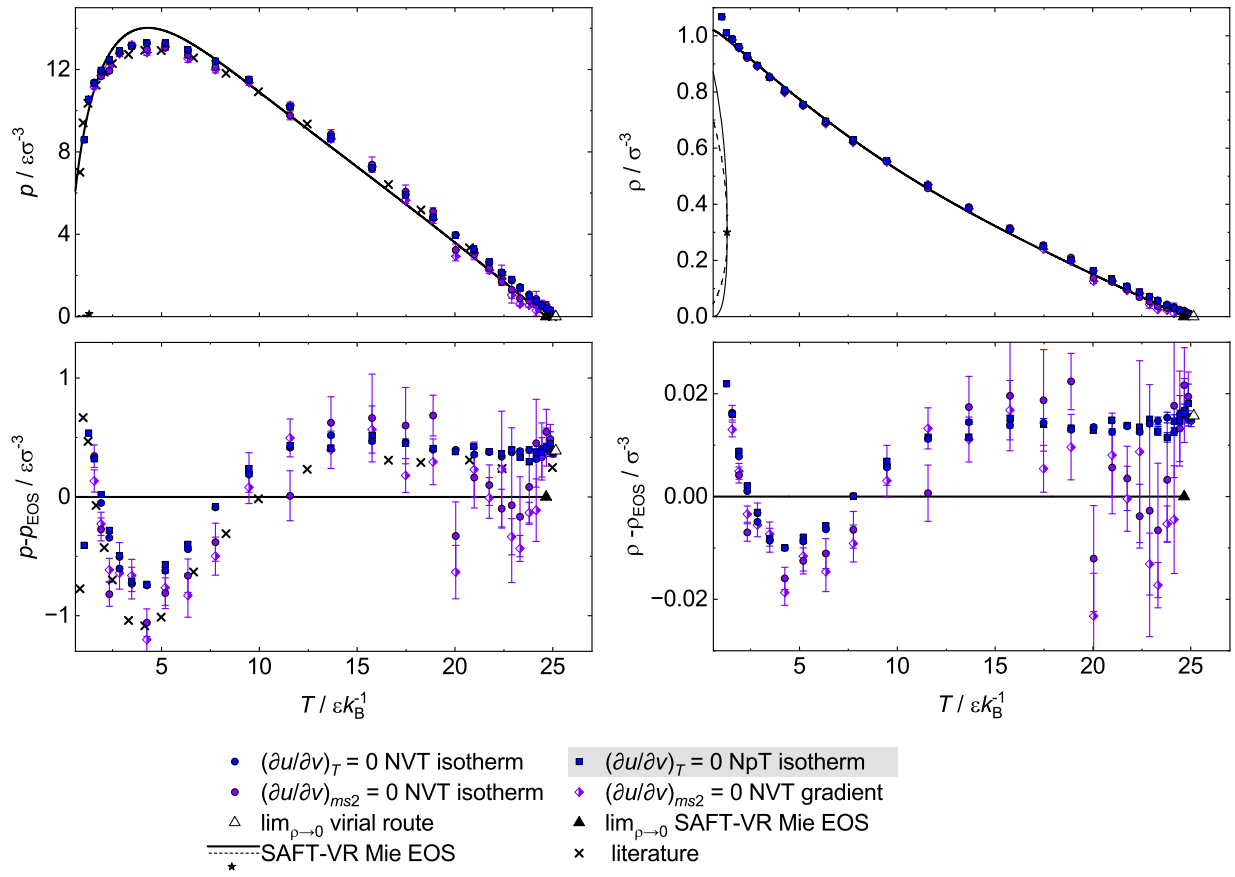

Figure S5: Results for the Amagat curve of the Lennard-Jones fluid. Left: Pressure-temperature projection; Right: Density-temperature projection. Purple and blue symbols indicate the simulation results from this work; black crosses the results from *Deiters & Neumaier*[1] taken from the LJ database.[2] Thick solid line and filled black triangle indicate the EOS initial guess value for the Amagat curve. The open triangle indicates the zero-density limit Zeno curve state point obtained from the virial route. The bottom row shows the deviation plots using the EOS results as a base line. In the deviation plots, for data points located at higher temperatures than the zero-density limit of the EOS, a linear extrapolation of the EOS results was applied. Thin Dashed lines, thin solid lines, and filled star indicate the EOS[3] results for the VLE binodal, spinodal, and critical point, respectively.

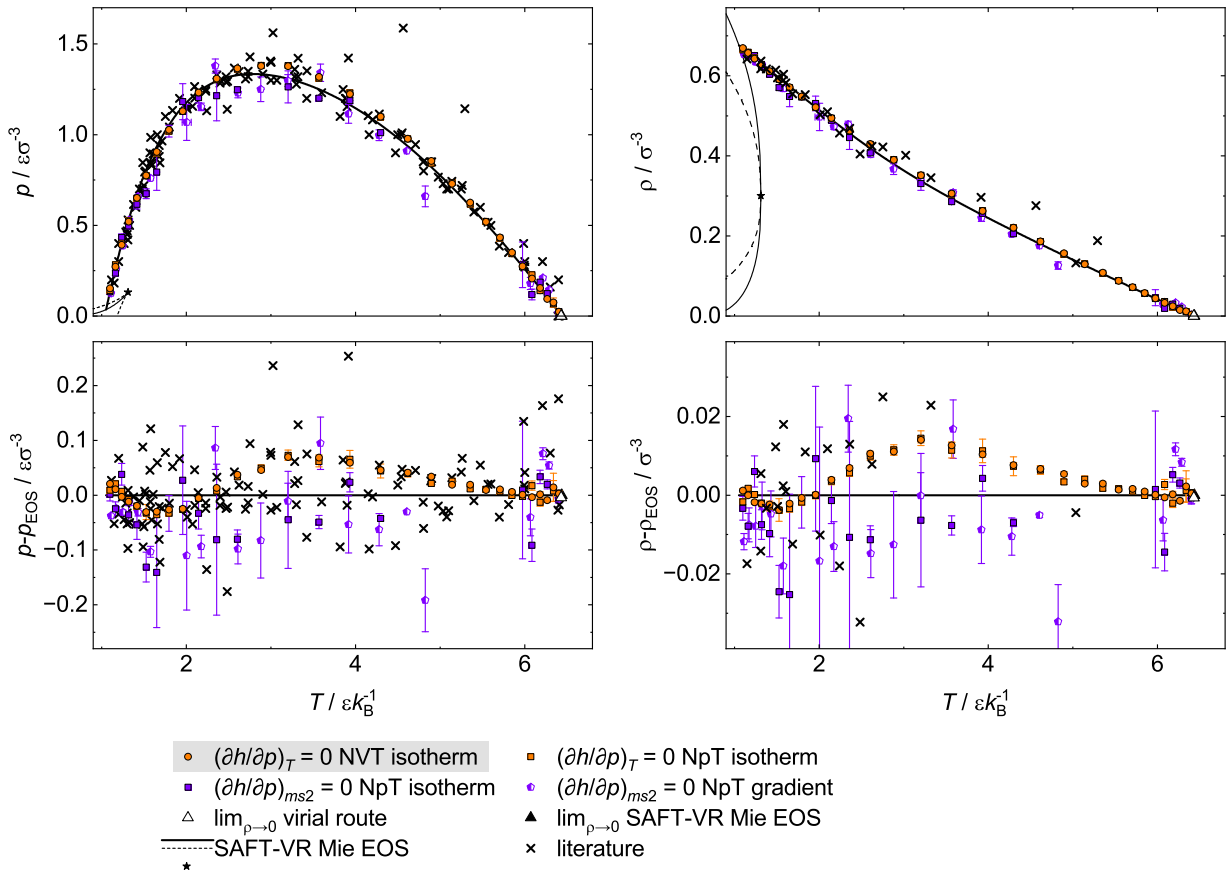

Figure S6: Results for the Charles curve of the Lennard-Jones fluid. Left: Pressure-temperature projection; Right: Density-temperature projection. Orange and purple symbols indicate the simulation results from this work; black crosses results from the literature[4–10] taken from the LJ database.[2] Error bars of literature data is not shown for clarity. Thick solid line and filled black triangle indicate the EOS initial guess value for the Charles curve. The open triangle indicates the zero-density limit Zeno curve state point obtained from the virial route. The bottom row shows the deviation plots using the EOS results as a base line. Thin Dashed lines, thin solid lines, and filled star indicate the EOS[3] results for the VLE binodal, spinodal, and critical point, respectively.

Detailed comparison to literature data for the Charles curve

Fig. S7 shows a detailed comparison of the results from this work to literature data available for the Charles curve of the Lennard-Jones fluid. For the results from this work, only the results from the overall most beneficial route are shown. Seven data sets for the Lennard-Jones Charles curve are available in the literature.[4–10] The data sets from Refs.[4,5,7,9] have reported uncertainties of the data. Density data for the Charles curve data points was reported by Refs.[4,5,7]

The results from *Heyes & Llaguno*[5] show large scattering and systematic deviations from all other data sets at high temperatures. The results from this work are in excellent agreement with the results from *Roesler et al.*[10] and also in reasonable agreement with the results from *Yigzawe & Sadus*,[7] *Deiters & Neumaier*,[1] *Kioupis et al.*,[4] and *Vrabec et al.*[9] The results from this work are in excellent agreement with the zero-density limit value (open triangle in Fig. S7) obtained from the virial route, which therefore can be considered the exact limit. Also the data sets of *Roesler et al.*[10] and *Kioupis et al.*[4] are in good agreement with the exact zero-density limit. The data set of *Deiters & Neumaier*[1] slightly systematically underestimates the data set from this work and the zero-density limit state point. The same holds for the data set of *Vrabec et al.*[9] for most temperatures. The results from *Colina & Müller*[6] overestimate the zero-density limit (and the results from this work in the vicinity of the zero-density limit), but underestimate the results from this work at moderate temperatures.

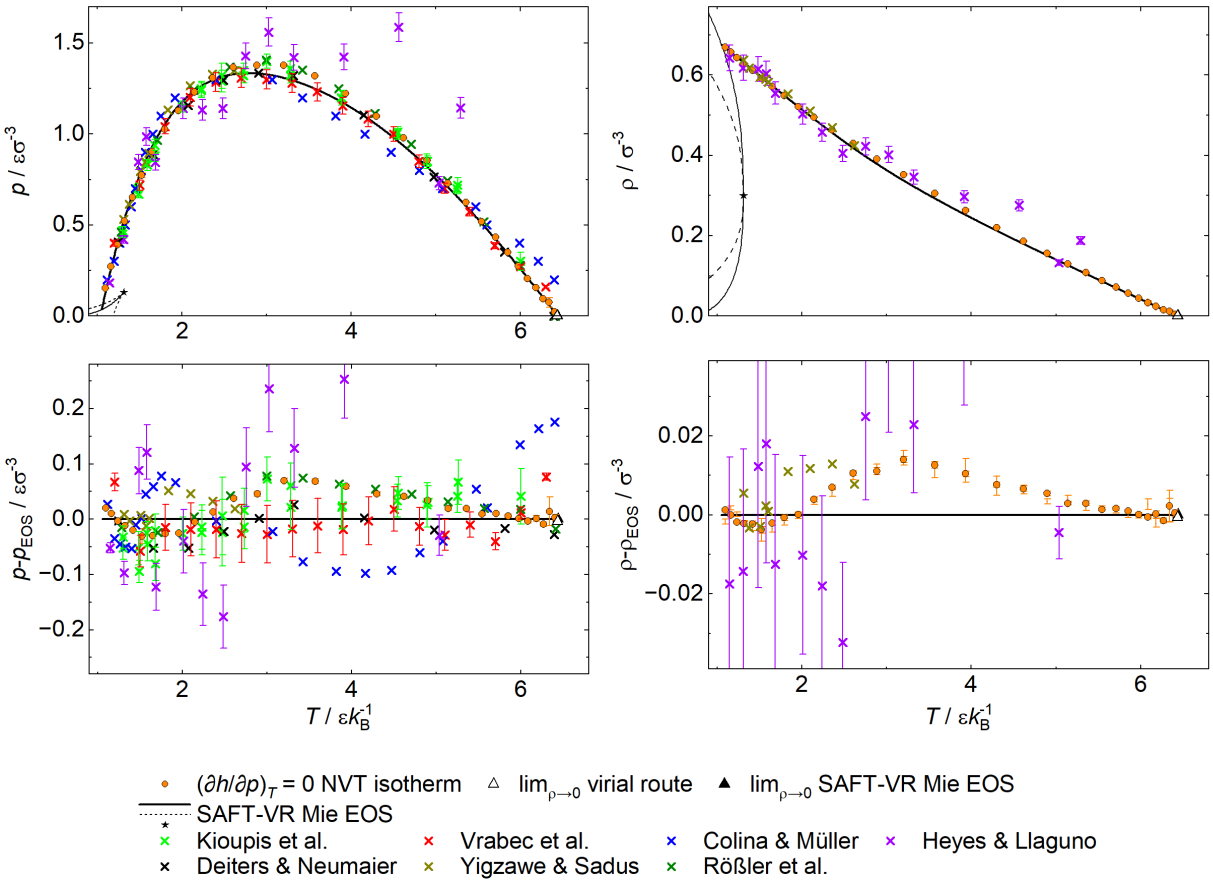

Figure S7: Results for the Charles curve of the Lennard-Jones fluid: Pressure-temperature projection (left) and the corresponding deviation plot (right) taking the EOS results as base line. Orange circles indicate the simulation results from this work; crosses indicate results from the literature[4–10] taken from the LJ database.[2] Thick solid line and filled black triangle indicate the EOS initial guess value for the Charles curve. The open triangle indicates the zero-density limit Charles curve state point obtained from the virial route. Thin Dashed lines, thin solid lines, and filled star indicate the EOS[3] results for the VLE binodal, spinodal, and critical point, respectively.

Simulation details and results for toluene, methane, ethane, propane, and ethanol

The initial guess values for the studied real substance fluids (toluene, ethane, propane, and ethanol) were determined using the SAFT-VR Mie EOS.[3] For methane, the Lennard-Jones fluid results were used using the methane model parameters proposed by *Vrabec et al.*[11] The model parameters for the substances toluene, ethane, propane, and ethanol used in the EOS were taken from Refs.[3,12] The parameters are summarized in Table S1.

The second virial coefficient of each substance was determined using MC simulations based on the respective force field as described in the main part of the paper. For toluene, the results for the second virial coefficient and the characteristic temperature values are shown in Fig. S8. The corresponding results for ethane, propane, and ethanol are given in the electronic spread sheets.

Based on the characteristic temperature values, the EOS initial guess data for the characteristic curves was corrected in the vicinity of the zero-density limit. For toluene, multiple simulation routes were applied and compared – only the 'gradient' simulation grid method was not considered as it is more complex than the other grid types, but did not yield any advantage for the LJ fluid. For ethane, propane, and ethanol, only the most favorable simulation route was applied.

Table S1: Model parameters used for the SAFT-VR Mie EOS taken from the literature.[3,11,12] The repulsive and attractive exponents are described by λ_r and λ_a, respectively. The chain length is indicated by m, the dispersion energy by ε, and the size parameter by σ. The association of ethanol was modeled as 2B association scheme in the denotation of Huang and Radosz.[13] The association strength is indicated by ε_{AB} and the association radius by r_{AB}.

	M / g mol^{-1}	$(\varepsilon/k_\mathrm{B})$/K	σ/Å	m	λ_r	λ_a	$(\varepsilon_{AB}/k_\mathrm{B})$/K	r_{AB}/σ
toluene	92.14	474.13	4.5487	1.7112	19.125	6		
methane	16.04	148.55	3.7281	1.0000	12	6		
ethane	30.07	206.12	3.7257	1.4373	12.4	6		
propane	44.10	239.89	3.9056	1.6845	13.006	6		
ethanol	46.07	168.15	3.4914	1.9600	7.6134	6	2833.7	0.34558

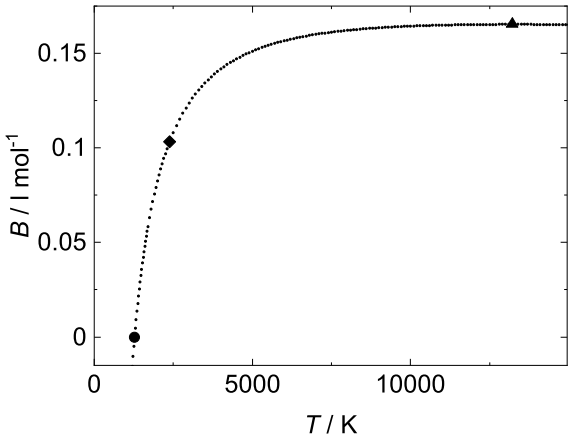

Figure S8: Results for the second virial coefficient of toluene obtained from the MC simulations carried out with *ms*2. The filled black circle indicates $B = 0$, the filled diamond indicates $\partial B/\partial T = B/T$, and the filled triangle indicates the maximum of B.

The virial-corrected EOS initial guess values were used for the setup of the simulation grid. For the scattering parameter, a relative distance between the data points of 3% in density and 8% in pressure was used. Up to 30 characteristic curve state points were determined for each of the four characteristic curves. For each characteristic curve state point, a set of seven simulations was carried out.

Fig. S9 shows the results of the Zeno curve for toluene. The results from all considered approaches show small scattering as well as small statistical uncertainties. Moreover, the results from the four data sets are in excellent agreement. Small deviations are only observed in the vicinity of the pressure maximum.

Fig. S10 shows the results of the Amagat curve for toluene. The results from both approaches based on the condition $(\partial u/\partial v)_T = 0$ are in good agreement with the zero-density limit state point. Moreover, the results from both approaches show a smooth trend and relatively small statistical uncertainties. The results from the NVT isothermal approach slightly overestimate the results from the NpT isothermal approach in the vicinity of the pressure maximum. As for the LJ simulations, more stable simulation runs are observed in the high-density region for the NpT simulations compared to the NVT simulations.

Fig. S11 shows the results of the Boyle curve for toluene. The results from the Helmholtz

energy route exhibit large scattering, which is due to the fact that $\tilde{a}_{02}$ is challenging to sample with high accuracy. The results from the four approaches based on a condition using a derivative of the compressibility factor with respect to pressure or volume, on the other hand, show small scattering and small error bars. Also, the results from these four approaches are in excellent agreement with the zero-density limit obtained from the virial route. However, significant deviations between the results from these four approaches are observed in the vicinity of the vapor-liquid equilibrium. Only the approach $(\partial Z/\partial v)_T = 0$ NVT in the isothermal setup yields reliable results – especially in the metastable region.

Fig. S12 shows the results of the Charles curve for toluene. Again, the results from the Helmholtz energy route exhibit large scattering. The same holds for the $(\partial h/\partial p)_{\mathrm{ms2}} = 0$ approach, which was directly sampled in $ms2$. The isobaric simulation sets using the $(\partial Z/\partial T)_p = 0$ and $(\partial Z/\partial v)_p = 0$ condition yield erratic results (not shown in Fig. S12) in the vicinity of the pressure maximum. Both approaches based on the condition $(\partial h/\partial p)_T = 0$ yield good results, i.e. a smooth trend and small statistical uncertainties as well as good agreement with the zero-density limit value obtained from the virial route.

The approaches identified in the main body of the this work to be the overall most favorable approach for determining the four characteristic curves also yield very good results for toluene. The four most beneficial approaches were identified as $Z = 1$ in NVT simulations for the Zeno curve, $(\partial u/\partial v)_T = 0$ in NpT simulations for the Amagat curve, $(\partial Z/\partial v)_T = 0$ in NVT simulations for the Boyle curve, and $(\partial h/\partial p)_T = 0$ in NVT simulations for the Charles curve. The results from these four approaches for the individual characteristic curves are in excellent agreement with the respective zero-density limit, cf. Fig. S9 - S12. Moreover, the results from these four approaches show relatively small scattering and small statistical uncertainties compared to the other studied approaches. This confirms the findings from the Lennard-Jones fluid results that these four approaches are the most robust and reliable ones for determining the respective characteristic curve.

Fig. S13 shows the Helmholtz energy derivative condition for the four characteristic curves

obtained from the final simulation at the characteristic curve state points based on the four approaches that were identified to yield the overall most favorable results. Only for the Zeno curve, some systematic deviations are observed in the vicinity of the pressure maximum of the curve. For the Amagat, Boyle and Charles curve, the vast majority of the data points confirm the thermodynamic consistency test.

Figs. S14 - S16 show the Helmholtz energy derivative condition for ethanol, ethane, and propane. Results are shown for all four characteristic curves obtained from the final simulation at the characteristic curve state points. The vast majority of results agrees reasonably well with the thermodynamic condition.

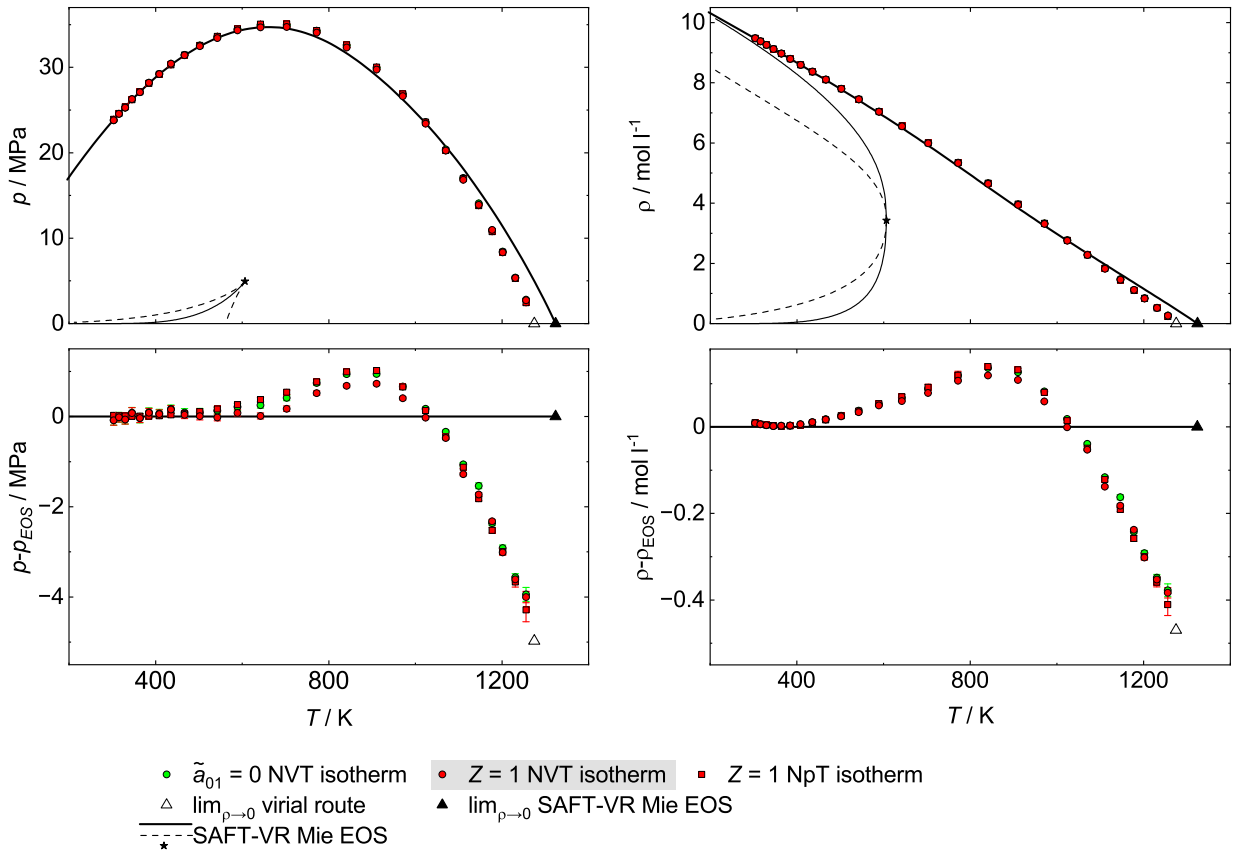

Figure S9: Results for the Zeno curve of toluene. Left: Pressure-temperature projection; Right: Density-temperature projection. Red and green symbols indicate the simulation results. Thick solid line and filled black triangle indicate the EOS initial guess value for the Zeno curve. The open triangle indicates the zero-density limit Zeno curve state point obtained from the virial route. The bottom row shows the deviation plots using the EOS results as a base line. Thin dashed lines, thin solid lines, and filled star indicate the EOS[3] results for the VLE binodal, spinodal, and critical point, respectively.

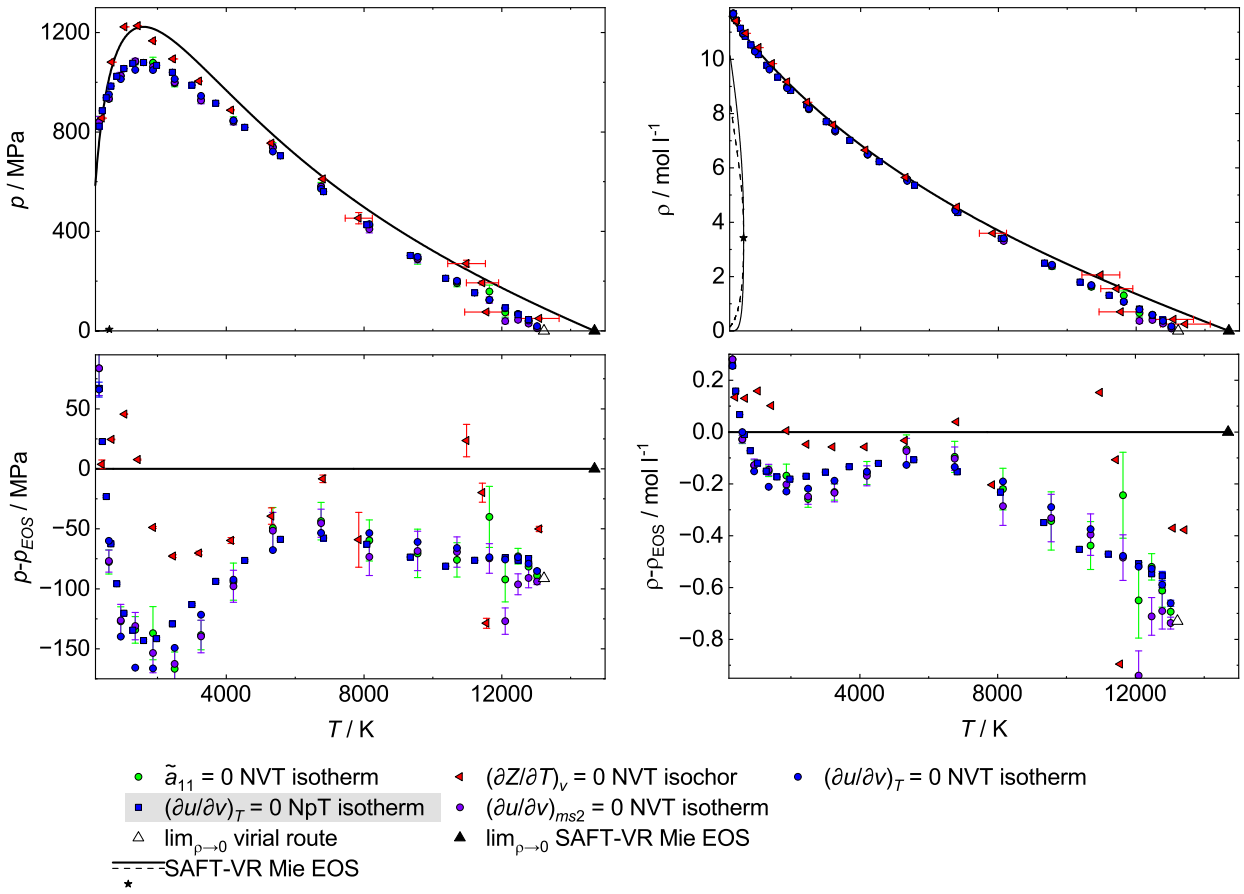

Figure S10: Results for the Amagat curve of toluene. Left: Pressure-temperature projection; Right: Density-temperature projection. Colored symbols indicate the simulation results. Thick solid line and filled black triangle indicate the EOS data for the Amagat curve. The open triangle indicates the zero-density limit Amagat curve state point obtained from the virial route. The bottom row shows the deviation plots using the EOS results as a base line. Thin dashed lines, thin solid lines, and filled star indicate the EOS[3] results for the VLE binodal, spinodal, and critical point, respectively.

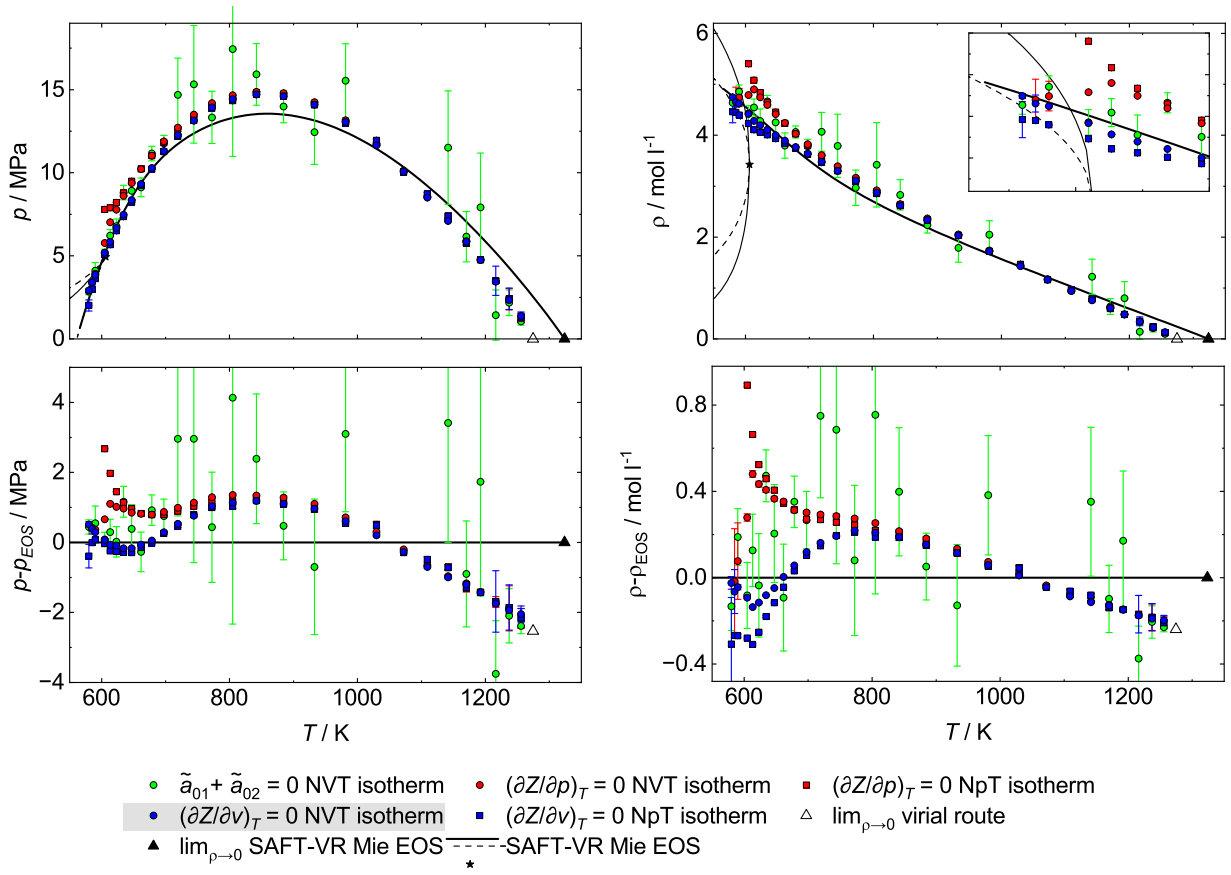

Figure S11: Results for the Boyle curve of toluene. Left: Pressure-temperature projection; Right: Density-temperature projection. Red, green, and blue symbols indicate the simulation results. Thick solid line and filled black triangle indicate the EOS data for the Boyle curve. The open triangle indicates the zero-density limit Boyle curve state point obtained from the virial route. The bottom row shows the deviation plots using the EOS results as a base line. Thin dashed lines, thin solid lines, and filled star indicate the EOS[3] results for the VLE binodal, spinodal, and critical point, respectively.

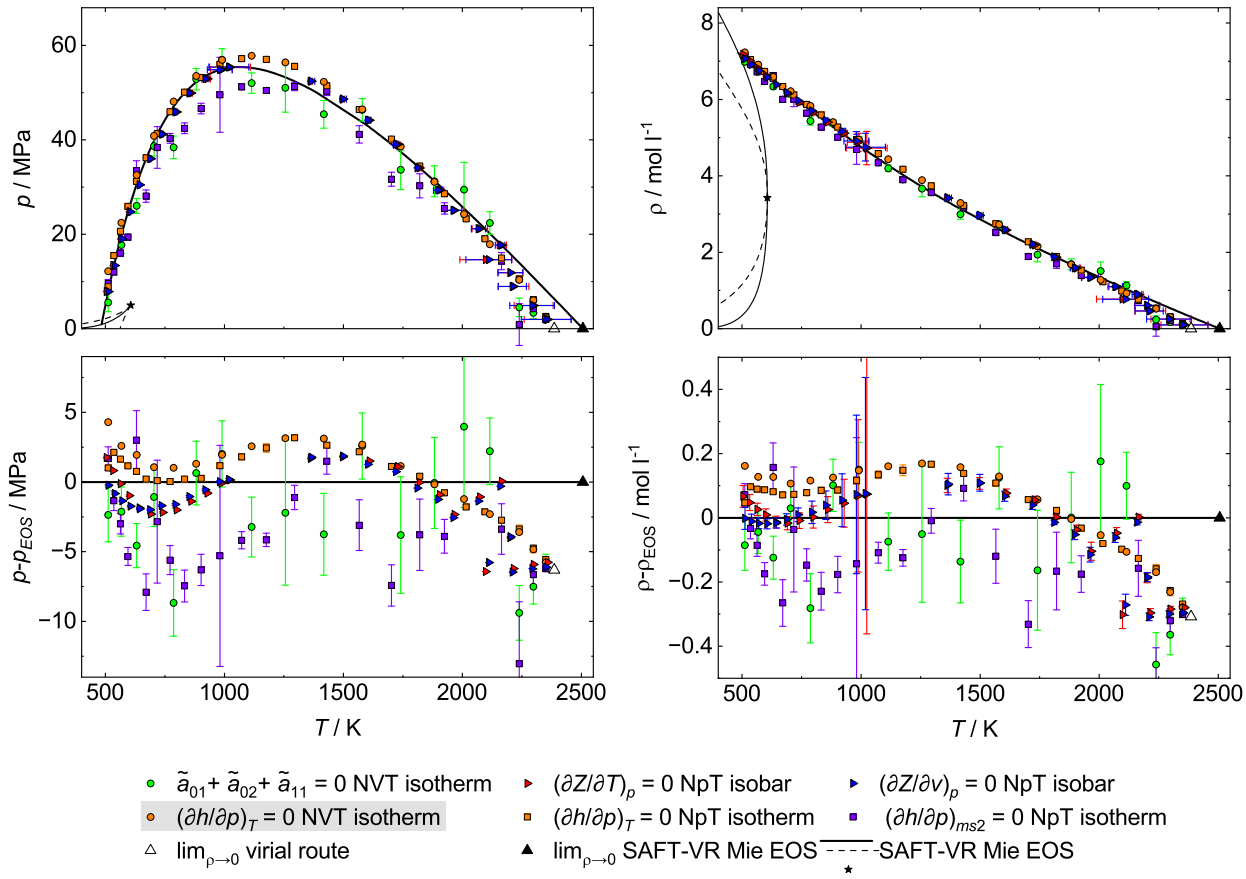

Figure S12: Results for the Charles curve of toluene. Left: Pressure-temperature projection; Right: Density-temperature projection. Colored symbols indicate the simulation results. Thick solid line and filled black triangle indicate the EOS data for the Charles curve. The open triangle indicates the zero-density limit Charles curve state point obtained from the virial route. The bottom row shows the deviation plots using the EOS results as a base line. Thin dashed lines, thin solid lines, and filled star indicate the EOS[3] results for the VLE binodal, spinodal, and critical point, respectively.

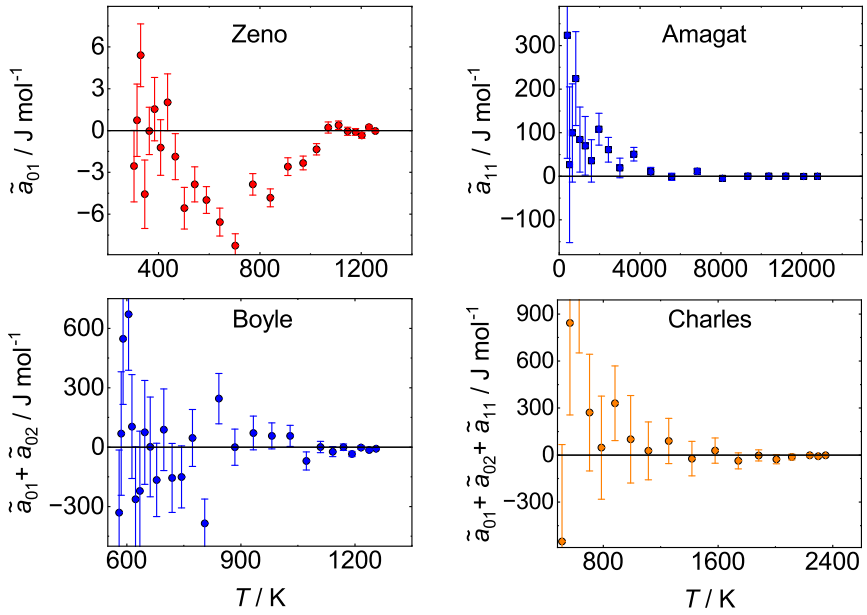

Figure S13: Consistency test for the Helmholtz energy criteria using the toluene results from the final simulations at the determined characteristic curve state points. Only results shown for the most favorable approach for each curve.

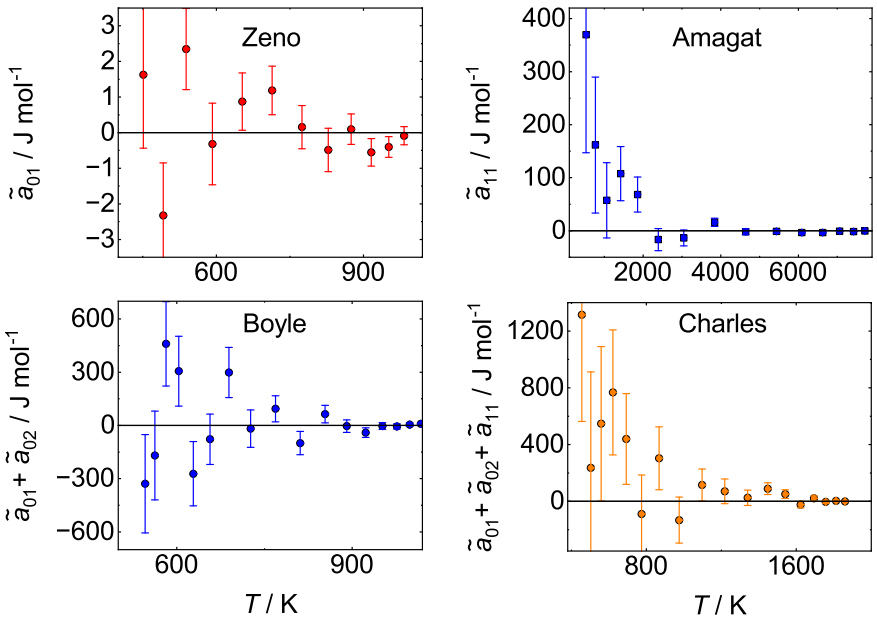

Figure S14: Consistency test for the Helmholtz energy criteria using the ethanol results from the final simulations at the determined characteristic curve state points.

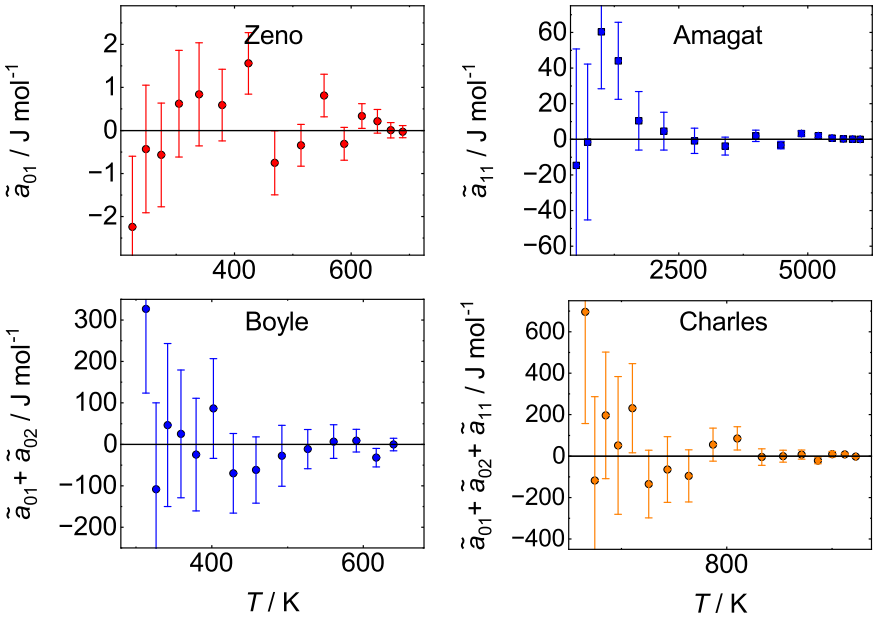

Figure S15: Consistency test for the Helmholtz energy criteria using the ethane results from the final simulations at the determined characteristic curve state points.

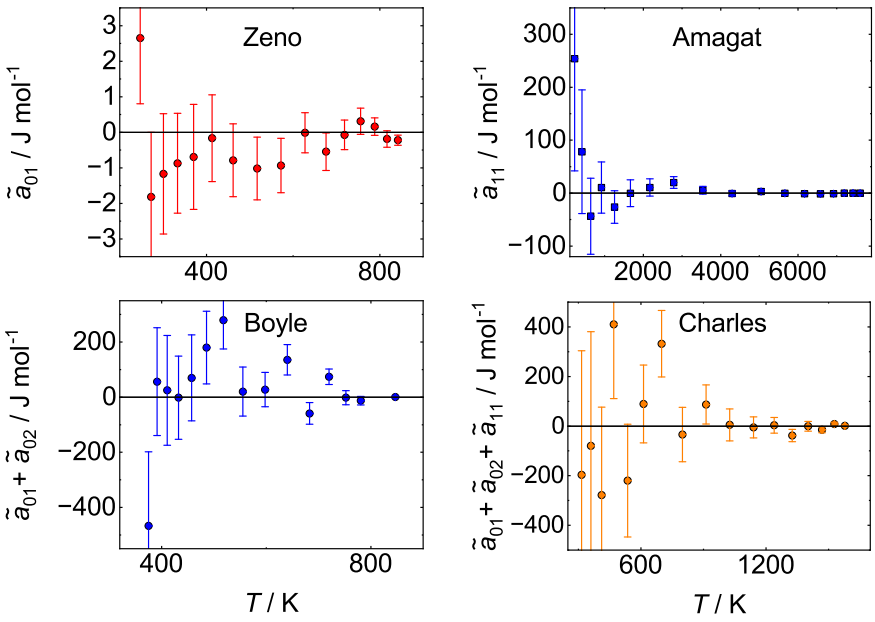

Figure S16: Consistency test for the Helmholtz energy criteria using the propane results from the final simulations at the determined characteristic curve state points.

Results for the Lennard-Jones truncated and shifted fluid

The third fluid studied in this work is the Lennard-Jones truncated and shifted (LJTS) fluid. An obvious choice for an EOS for computing initial guess data for the characteristic curves would be the PeTS EOS.[14] However, the PeTS EOS yields an erratic Amagat curve. Therefore, the corresponding state principle was applied to convert initial guess data computed from the SAFT-VR Mie EOS for the LJ fluid to the LJTS fluid. Hence, the characteristic curve data computed for the LJ fluid from the SAFT-VR Mie EOS was scaled based on the critical data of the LJ fluid and LJTS fluid:[15]

$$T_{\mathrm{LJTS}} = \frac{T_{\mathrm{c,LJTS}}}{T_{\mathrm{c,LJ}}} T_{\mathrm{LJ}} \qquad p_{\mathrm{LJTS}} = \frac{p_{\mathrm{c,LJTS}}}{p_{\mathrm{c,LJ}}} p_{\mathrm{LJ}} \qquad \rho_{\mathrm{LJTS}} = \frac{\rho_{\mathrm{c,LJTS}}}{\rho_{\mathrm{c,LJ}}} \rho_{\mathrm{LJ}} \ . \tag{1}$$

The grid of data points was specified by a distancing of data points of 3% in density and 8% in pressure. Up to 30 data points were determined for each characteristic curve and seven data points were used for each simulation set. The time step was $\Delta\tau = 0.001\,\sigma\sqrt{m/\varepsilon}$ and the cut-off radius was $r_{\mathrm{c}} = 2.5\sigma$. No long-range correction were applied, but the potential was shifted such that it was zero at the cut-off.

The results for the four characteristic curves are depicted in Figs. S17 - S20. Also the results from the PeTS EOS are shown for comparison. For all four characteristic curves, the initial guess data obtained from the corresponding states principle yields a good guess for the grid simulations such that the characteristic curve state points were obtained reliably.

Fig. S17 shows the results of the Zeno curve for the LJTS fluid. The results from the studied approaches show a smooth trend and relatively small error bars. Some scattering is only observed in the vicinity of the zero-density limit. There, the results from $Z = 1$ at isothermal conditions in the NVT ensemble yields the best agreement with the (exact) zero-density data point obtained from the virial route.

Fig. S18 shows the results of the Amagat curve for the LJTS fluid. The two data sets obtained for the condition $(\partial u/\partial v)_T = 0$ show significantly lower scattering, smaller error bars, and better agreement with the zero-density limit value compared to the data from the other approaches. In the low-temperature limit, the NVT simulations were observed to be more unstable compared to the NpT simulations.

Fig. S19 shows the results of the Boyle curve for the LJTS fluid. The results from all four considered approaches show a smooth trend. Moreover, the results form the four approaches are in very good agreement at high temperatures. Yet, important differences are observed at low temperatures in the vicinity of the vapor-liquid equilibrium. Only the results from the $(\partial Z/\partial v)_T = 0$ condition obtained from isothermal NVT simulation sets show a realistic behavior in the metastable region.

Fig. S20 shows the results of the Charles curve for the LJTS fluid. The best results (smooth trend, small statistical uncertainties, and consistent with the zero-density limit state point) are obtained from the $(\partial h/\partial p)_T = 0$ condition from isothermal NVT or isothermal NpT simulation sets (orange data sets). Small differences between the results from the $(\partial h/\partial p)_T = 0$ condition sets (orange data sets) are observed. Yet, the results from the condition $(\partial h/\partial p)_T = 0$ from both the NVT and NpT ensemble are in good agreement to the zero-density limit data point.

Also for the LJTS fluid, the approaches identified in the main body of the this work to be the overall most favorable ones, yield good results for the characteristic curves. This confirms the findings from the LJ fluid and toluene.

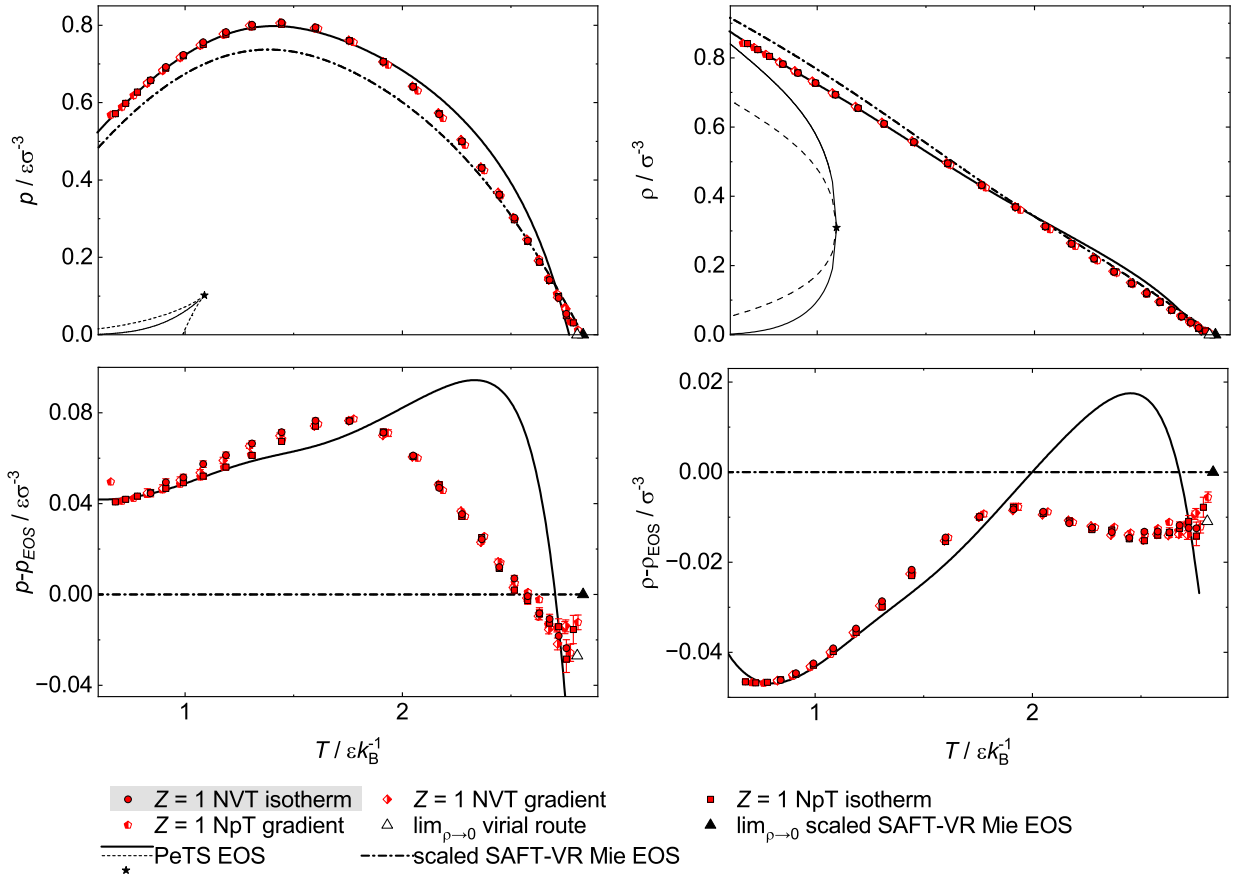

Figure S17: Results for the Zeno curve of the Lennard-Jones truncated and shifted fluid. Left: Pressure-temperature projection; Right: Density-temperature projection. Red symbols indicate the simulation results. The dot-dashed line and filled black triangle indicate the EOS[3] initial guess value for the Zeno curve. The open triangle indicates the zero-density limit Zeno curve state point obtained from the virial route. The bottom row shows the deviation plots using the EOS[3] results as a base line. Thin dashed lines, thin solid lines, and filled star indicate the PeTS EOS[14] results for the VLE binodal, spinodal, and critical point, respectively. The thick solid line indicates the PeTS results for the Zeno curve.

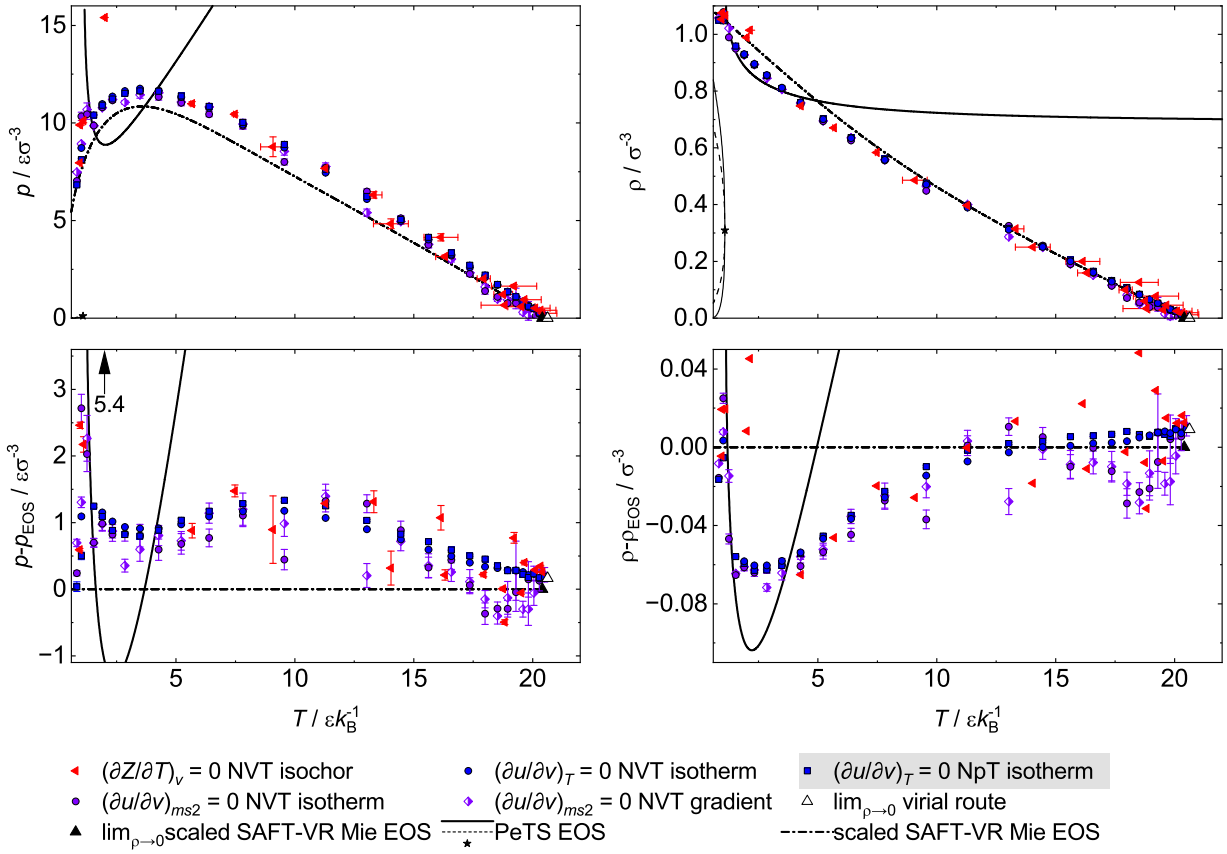

Figure S18: Results for the Amagat curve of the Lennard-Jones truncated and shifted fluid. Left: Pressure-temperature projection; Right: Density-temperature projection. Colored symbols indicate the simulation results. The dot-dashed line and filled black triangle indicate the EOS[3] initial guess value for the Amagat curve. The open triangle indicates the zero-density limit Amagat curve state point obtained from the virial route. The bottom row shows the deviation plots using the EOS[3] results as a base line. Thin dashed lines, thin solid lines, and filled star indicate the PeTS EOS[14] results for the VLE binodal, spinodal, and critical point, respectively. The thick solid line indicates the PeTS results for the Amagat curve.

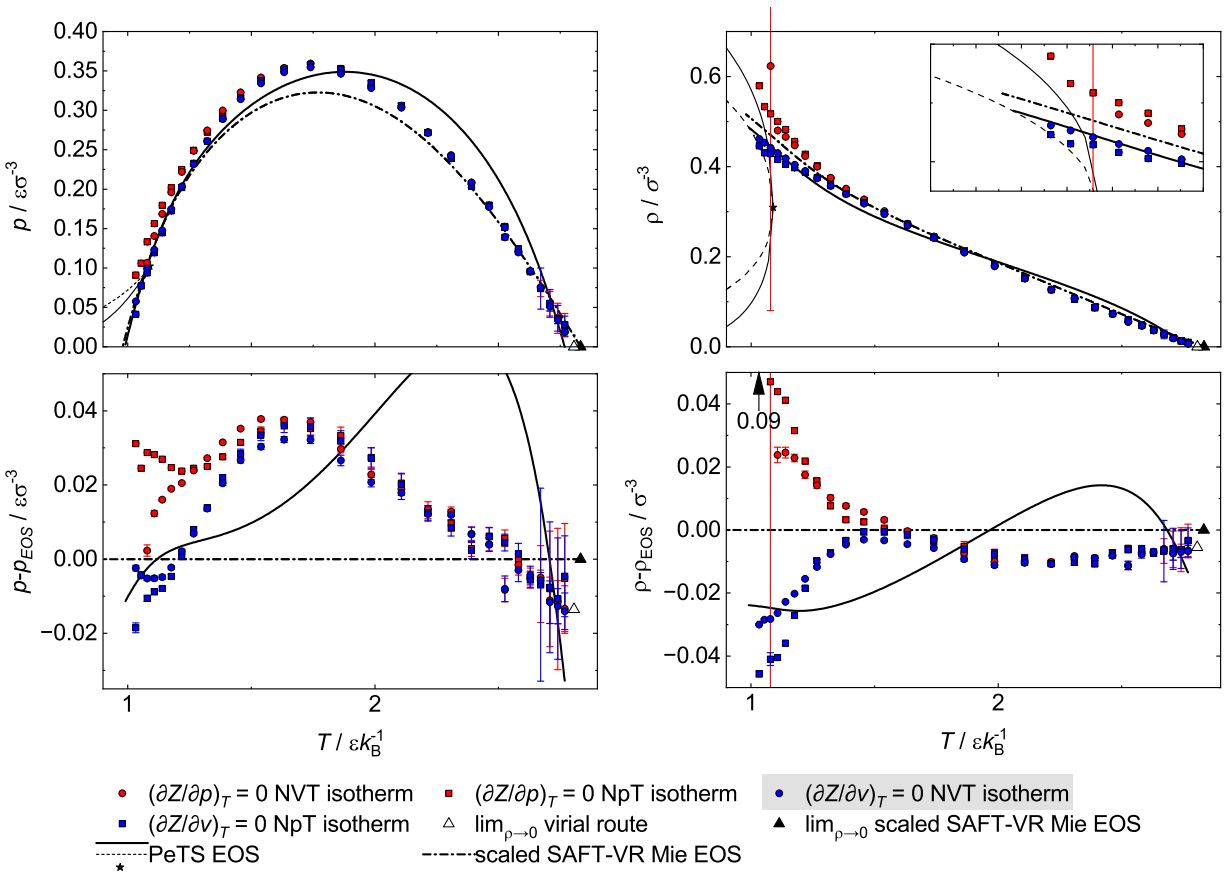

Figure S19: Results for the Boyle curve of the Lennard-Jones truncated and shifted fluid. Left: Pressure-temperature projection; Right: Density-temperature projection. Red and blue symbols indicate the simulation results. The dot-dashed line and filled black triangle indicate the EOS[3] initial guess value for the Boyle curve. The open triangle indicates the zero-density limit Boyle curve state point obtained from the virial route. The bottom row shows the deviation plots using the EOS[3] results as a base line. Thin dashed lines, thin solid lines, and filled star indicate the PeTS EOS[14] results for the VLE binodal, spinodal, and critical point, respectively. The thick solid line indicates the PeTS results for the Boyle curve.

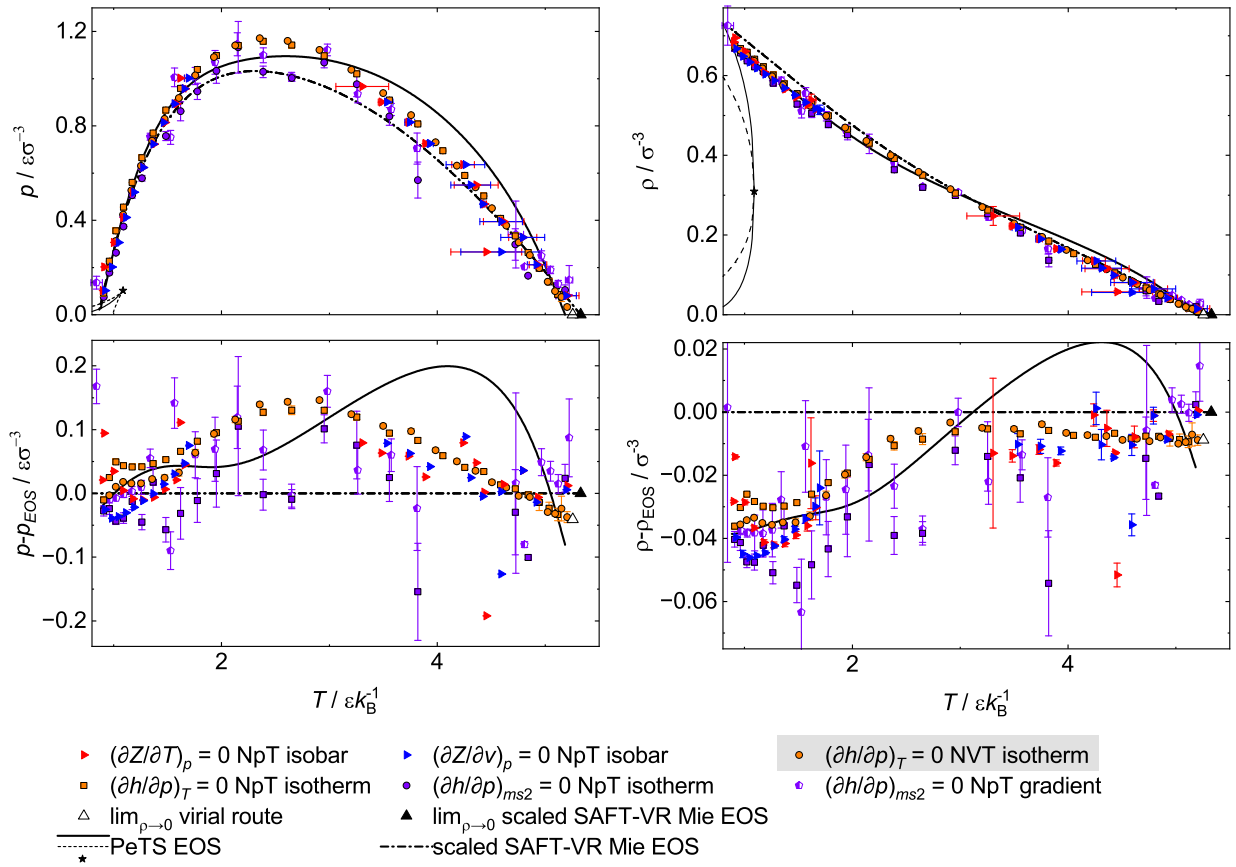

Figure S20: Results for the Charles curve of the Lennard-Jones truncated and shifted fluid. Left: Pressure-temperature projection; Right: Density-temperature projection. Colored symbols indicate the simulation results. The dot-dashed line and filled black triangle indicate the EOS[3] initial guess value for the Charles curve. The open triangle indicates the zero-density limit Charles curve state point obtained from the virial route. The bottom row shows the deviation plots using the EOS[3] results as a base line. Thin dashed lines, thin solid lines, and filled star indicate the PeTS EOS[14] results for the VLE binodal, spinodal, and critical point, respectively. The thick solid line indicates the PeTS results for the Charles curve.

Testing the linearity-law for the Zeno curve

Apfelbaum et al.[16,17] showed in their work that the Zeno curve of several real substances exhibit a linear behavior in the ρ-T projection. Initially, this was discovered by *Batschinski*.[18] Here, the first principle simulation results from this work are used to test the linearity-law. Only the results from the condition $Z = 1$ obtained from isothermal NVT simulation sets were used for that test.

Fig. S21 shows the results for the Lennard-Jones fluid and Fig. S22 shows the results for toluene. A linear fit was parameterized to the molecular simulation results from the two fluids using the zero-density limit state point as anchor. It is thereby shown that the molecular simulation results from this work confirm the linearity law reasonably well. Nevertheless, the simulation results (that are considered as a reference here) show some deviations from the linear behavior. These deviations exceed the uncertainties of the molecular simulation results. Hence, the linearity-law should be considered an approximation instead of a rigorous physical law.

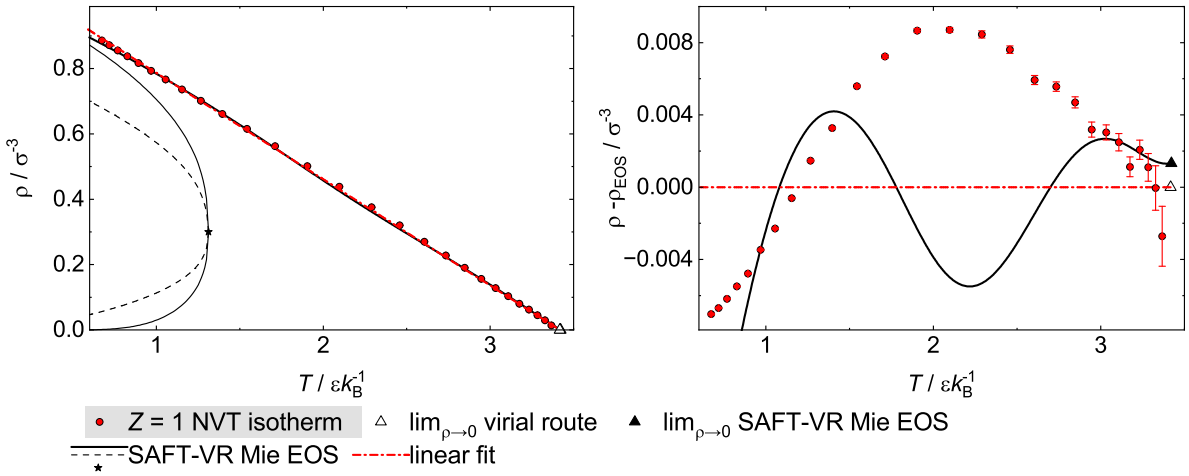

Figure S21: Test of the linearity-law for the Zeno curve. Results for the Lennard-Jones fluid. Red symbols indicate simulation results. The red line indicates a linear fit to the simulation results using the zero-density limit state point as anchor. Other lines and symbols are results from the SAFT-VR Mie EOS.

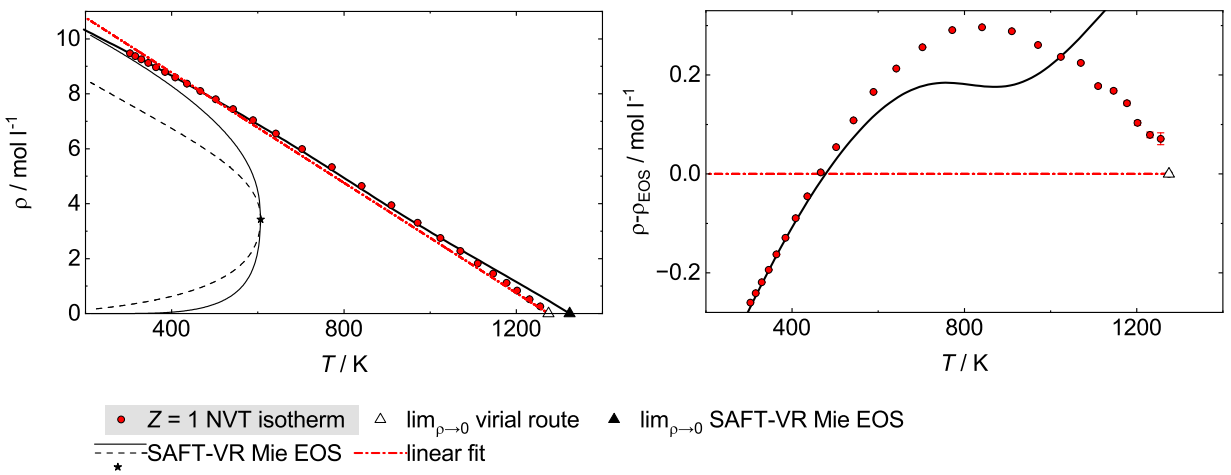

Figure S22: Test of the linearity-law for the Zeno curve. Results for toluene. Red symbols indicate simulation results. The red line indicates a linear fit to the simulation results using the zero-density limit state point as anchor. Other lines and symbols are results from the SAFT-VR Mie EOS.

Electronic Supporting Information – implementation of computational procedure

The electronic Supporting Information contains the implementation of the algorithm proposed in this work for determining Brown's characteristic curves. The scripts are implemented in Matlab and in shell. The core of the implementation are the scripts `PreProcessing.m`, `CreateParFiles.sh`, `PostProcessing.m`, and `Evaluation.m`. In each script, all settings that can be made by the user are marked in the section-header: `main settings(user input)`. Moreover, the script `IntegralVirial.m` is provided that can be used for calculating the second virial coefficient from simple model fluids by numerical integration of the potential. The file `SlurmOptions.sh` contains example settings that can be conveniently used on a SLURM system for launching the simulations. Also, example input and output files for all scripts are provided. All example algorithm input and output files are provided under the path `implementation/exampleFiles/`.

In the first part of the algorithm for the calculation of the second virial coefficient, the `PreProcessing.m` script generates a `.csv` file with temperature values to be used in the

MC simulations. Therefore, the user has to set `MODE = 1` and specify the temperature range and step size dT as input. An example for the generated `.csv` file is given in the electronic Supporting Information.

The `.csv` file containing the temperature values is read in by the `createParFiles.sh` shell script, which generates separate `.par` files for each temperature that can be straightforwardly used as *ms*2 input files. Therefore, a template `.par` file is required, which is also given in the `exampleFiles` folder. For the simulation, also a `.pm` file with the molecular model force field parameters is required. A sample file is also provided in the `exampleFiles` folder. The `createParFiles.sh` shell script moreover provides the possibility to send the generated `.par` files directly to the scheduler of a given machine. Therefore, the SLURM options have to be defined in a separate `SlurmOptions.sh` file. For further information to the usage of SLURM the reader is referred to the SLURM documentation, e.g. `https://www.schedmd.com`. Once the second virial coefficient simulations ended, the simulation result files are given to the `PostProcessing.m` script as input. This script reads the result files and generates a `.xlsx` file with the required output values. The results should exactly match the format of the example file from the `exampleFiles` folder to avoid errors in the subsequent scripts. The evaluation script computes the specific points of the second virial coefficient corresponding to the zero-density limit state points of the characteristic curves. For this purpose, the correlation of *Xu et al.*[19] was used. As described in the main body of this work, the specific points of the second virial coefficient for simple spherical model potentials can be calculated from numerical integration, which can be carried out by the script `IntegralVirial.m`.

In the second part of the algorithm (`MODE = 2` for all Matlab scripts), the characteristic curve state points are determined using first the `PreProcessing.m` script, which requires estimate state points of the characteristic curves as input. These initial guess values can be computed from various molecular-based equations of state available in the literature. The file `EXAMPLEOutput_EOS_VirialCoeff.xlsx` gives an example of the syntax used in the implementation. The `EOS_data` sheet includes the results of the EOS. The format of

the data is mandatory for the further scripts and has to be adopted by the user. The `Virial_intermolecularPotential` sheet contains the data of the virial coefficient and has the same format as the output file of the `Evaluation.m` script or the `IntegralVirial.m` script. In the next step, the `PreProcessing.m` script requires further input from the user, namely, (a) the arrangement of the simulation sets for each characteristic curve, (b) the number of simulation points N_{set}, (c) the number of sample points N_{sim}, (d) the scattering width of the sets L_{NVT} or L_{NpT}, and (e) the reference units to reduce mass and length if SI units are used (this is a feature of $ms2$ and may differ for other simulation engines). As an output, the `PreProcessing.m` script provides a `.csv` file containing the simulation grid state points and eventually the piston mass. In addition, an associated `.idf` file (identifier file) is created for each curve. The `.idf` file contains the information, which grid state points of the `.csv` file belong to a simulation set. The actual molecular simulations can again be launched using the `CreateParFiles.sh` shell script. Therefore, also a template `.par` file is required (an example is provided in the electronic Supporting Information). Also, the SLURM option can be used in this step. For the `PostProcessing.m` script, the simulation ensemble has to be specified by the user such that the appropriate post-processing is carried out. The `PostProcessing.m` script reads the simulation results `.res` and `.log` files and also the `.csv` and `.idf` input files (all these files have to be in the same folder). The `PostProcessing.m` script creates a `.xlsx` file as output. The `Evaluation.m` script computes the characteristic curve state points from the simulation results as described in the main body of this work. The user can decide, which condition is to be used to evaluate the characteristic curves (to be in accordance with the simulation grid type and ensemble). During the evaluation process, several plots are generated by the script that enable a visual inspection of the results. If different methods for the evaluation of the same characteristic curve are to be compared, the script `CompareResults.m` can be used. This is optional in a sense that it is not mandatory in the algorithm workflow.

An important part of the proposed computational procedure is the generation of the

simulation grid. The implemented grid generator can be used to generate different grid types. Also, multiple simulation parameters can be specified. One setting of the grid generator is the width of the scattering of the simulation state points, which can be specified by the parameter L indicating the distance between the points in a set in density (for NVT ensemble) or in pressure (for NpT ensemble). The distance is described as a relative value with respect to the maximum density or pressure value computed by the EOS. The grid generator uses several heuristic functions to generate a grid of simulation state points. To avoid simulations in the unstable region (as predicted by the EOS), the grid generator reduces the scattering of the simulation state points (in the NVT ensemble) L_{NVT} such that no simulation state point lies in the unstable region. To account for larger differences in fluid compressibility in the different state regions, the scattering between the simulation points of an NVT set is also adjusted in the low-temperature and high-temperature region. For this purpose, for the Zeno curve in the temperature range smaller than 1.3 T_{crit}, the scattering is reduced step-wise by up to 95%. For the Amagat curve, the scattering is reduced step-wise in the temperature range smaller than 1.5 T_{crit} up to 50%. For the Boyle curve, the scattering is increased up to 170% in the temperature region smaller than 2 T_{crit} and reduced by up to 90% above 2 T_{crit}. No adjustment is applied for the Charles curve. The distance between the simulation sets is decreased in the vicinity of both the zero-density limit and the low-temperature limit. For this purpose, the density of the arrangement of the simulation sets is increased by means of an exponential function starting at the mean temperature between the zero-density limit and the low-temperature limit of the characteristic curve up to these end points. Also, the algorithm circumvents configurations where the scattering of the simulation points yield simulation points with negative density or negative pressure.

In the third part of the algorithm (`MODE = 3` for all Matlab scripts), final simulations at the estimated characteristic curve state points are carried out. The `PreProcessing.m` script requires the general input the EOS data file (which is the same as in part 2) and the output of the prior `Evaluation.m` script calls. Furthermore, also the reference mass and unit length

are required, if SI units are used. Here, also a `.csv` and `.idf` file is generated, which is then to be used to create `.par` files with the `CreateParFiles.sh` shell script. As in the previous steps, a template `.par` file is required. The SLURM option can also be used in this part. After the simulations are carried out, the results are compiled by the `PostProcessing.m` script and the data is written to a `.xlsx` file. The ensemble used in the simulations has to be specified to the `PostProcessing.m` script as well as the input `.csv` and `.idf` file and the `.res` and `.log` files.

Electronic Supporting Information – simulation results

The electronic Supporting Information contains three types of `.xlsx` spreadsheets for each fluid. The results for Brown's characteristic curves obtained from the different approaches are in the files `Results_Evaluation_Simulation#2_fluidname.xlsx` and the results of the final simulations at the obtained characteristic curve state points are provided in the files `Results_Simulation#3_fluidname.xlsx`. Moreover, the primary data of all simulations carried out using the different grid types and used for the evaluation of the characteristic curve state points are provided in the files `Results_SimulationGrid_curve_grid-type.xlsx`. Furthermore, the results for the second virial coefficient of the three fluids are provided in the file `Results_VirialCoefficients.xlsx`.

References

(1) Deiters, U. K.; Neumaier, A. Computer Simulation of the Characteristic Curves of Pure Fluids. *J. Chem. Eng. Data* **2016**, *61*, 2720–2728.

(2) Stephan, S.; Thol, M.; Vrabec, J.; Hasse, H. Thermophysical Properties of the Lennard-Jones Fluid: Database and Data Assessment. *J. Chem. Inf. Model.* **2019**, *59*, 4248–4265.

(3) Lafitte, T.; Apostolakou, A.; Avendano, C.; Galindo, A.; Adjiman, C. S.; Müller, E. A.; Jackson, G. Accurate Statistical Associating Fluid Theory for Chain Molecules formed from Mie Segments. *J. Chem. Phys.* **2013**, *139*, 154504.

(4) Kioupis, L. I.; Arya, G.; Maginn, E. J. Pressure-Enthalpy Driven Molecular Dynamics for Thermodynamic Property Calculation II: Applications. *Fluid Phase Equilib.* **2002**, *200*, 93–110.

(5) Heyes, D. M.; Llaguno, C. T. Computer Simulation and Equation of State Study of the Boyle and Inversion Temperature of Simple Fluids. *Chem. Phys.* **1992**, *168*, 61–68.

(6) Colina, C. M.; Müller, E. A. Molecular Simulation of Joule-Thomson Inversion Curves. *Int. J. Thermophys.* **1999**, *20*, 229–235.

(7) Yigzawe, T. M.; Sadus, R. J. Intermolecular Interactions and the Thermodynamic Properties of Supercritical Fluids. *J. Chem. Phys.* **2013**, *138*, 194502.

(8) Deiters, U. K.; Neumaier, A. Computer Simulation of the Characteristic Curves of Pure Fluids. *J. Chem. Eng. Data.* **2016**, *61*, 2720–2728.

(9) Vrabec, J.; Kedia, G. K.; Hasse, H. Prediction of Joule-Thomson inversion curves for pure fluids and one mixture by molecular simulation. *Cryogenics* **2005**, *45*, 253–258.

(10) Rößler, J.; Antolovic, I.; Stephan, S.; Vrabec, J. Assessment of thermodynamic models via Joule-Thomson inversion. *Fluid Phase Equilib.* **2022**, *556*, 113401.

(11) Vrabec, J.; Stoll, J.; Hasse, H. A Set of Molecular Models for Symmetric Quadrupolar Fluids. *The Journal of Physical Chemistry B* **2001**, *105*, 12126–12133.

(12) Dufal, S.; Lafitte, T.; Galindo, A.; Jackson, G.; Haslam, A. J. Developing intermolecular-potential models for use with the SAFT-VR Mie equation of state. *AIChE J.* **2015**, *61*, 2891–2912.

(13) Huang, S. H.; Radosz, M. Equation of state for small, large, polydisperse, and associating molecules. *Ind. Eng. Chem. Res.* **1990**, *29*, 2284–2294.

(14) Heier, M.; Stephan, S.; Liu, J.; Chapman, W. G.; Hasse, H.; Langenbach, K. Equation of State for the Lennard-Jones Truncated and Shifted Fluid with a Cut-Off Radius of 2.5σ Based on Perturbation Theory and its Applications to Interfacial Thermodynamics. *Mol. Phys.* **2018**, *116*, 2083–2094.

(15) Stephan, S.; Liu, J.; Langenbach, K.; Chapman, W. G.; Hasse, H. Vapor-Liquid Interface of the Lennard-Jones Truncated and Shifted Fluid: Comparison of Molecular Simulation, Density Gradient Theory, and Density Functional Theory. *J. Phys. Chem. C* **2018**, *122*, 24705–24715.

(16) Apfelbaum, E. M.; Vorob'ev, V. S.; Martynov, G. A. Virial Expansion Providing of the Linearity for a Unit Compressibility Factor. *J. Phys. Chem. A* **2004**, *108*, 10381–10385.

(17) Apfelbaum, E. M.; Vorob'ev, V. S.; Martynov, G. A. Triangle of Liquid-Gas States. *J. Phys. Chem. B* **2006**, *110*, 8474–8480.

(18) Batschinski, A. Abhandlungen über Zustandsgleichung; Abh. I: Der orthometrische Zustand. *Ann. Phys.* **1906**, *324*, 307–309.

(19) Xu, L.; Duan, Y.-Y.; Liu, H.-T.; Yang, Z. Empirical correlations for second virial coefficients of nonpolar and polar fluids covering a wide temperature range. *Fluid Phase Equilib.* **2021**, *539*, 113032.